Characterizing molecular motion in H_2O and H_3O^+ with dynamical instability statistics

Jason R. Green,[1] Thomas S. Hofer,[2] R. Stephen Berry,[3] and David J. Wales[4,a)]
[1]*Department of Chemistry, Northwestern University, 2145 Sheridan Road, Evanston, Illinois 60208-3100, USA*
[2]*Theoretical Chemistry Division, Institute of General, Inorganic and Theoretical Chemistry, Leopold-Franzens-University of Innsbruck, Innrain 52a, 6020 Innsbruck, Austria*
[3]*Department of Chemistry, The University of Chicago, Chicago, Illinois 60637, USA*
[4]*Department of Chemistry, University of Cambridge, Lensfield Road, Cambridge CB2 1EW, United Kingdom*

(Received 4 November 2010; accepted 18 October 2011; published online 14 November 2011)

Sets of finite-time Lyapunov exponents characterize the stability and instability of classically chaotic dynamical trajectories. Here we show that their sample distributions can contain subpopulations identifying different types of dynamics. In small isolated molecules these dynamics correspond to distinct elementary motions, such as isomerizations. Exponents are calculated from constant total energy molecular dynamics simulations of H_2O and H_3O^+, modelled with a classical, reactive, all-atom potential. Over a range of total energy, exponent distributions for these systems reveal that phase space exploration is more chaotic near saddles corresponding to isomerization and less chaotic near potential energy minima. This finding contrasts with previous results for Lennard-Jones clusters, and is explained in terms of the potential energy landscape. © *2011 American Institute of Physics*. [doi:10.1063/1.3658642]

I. INTRODUCTION

Highly vibrationally excited molecules exhibit chaotic classical dynamics, undergoing large-amplitude motion that leads to isomerization or the breaking of bonds. These dynamics, far from local minima of the potential energy surface, are not described by harmonic vibrational normal modes. This fact is a consequence of nonlinearly coupled degrees of freedom, which produce dynamical instability and chaos. New approaches are necessary to fully analyze these aspects of classical molecular dynamics. Lyapunov vectors, generalized analogs of normal mode vectors that are valid away from equilibrium points, are one such theoretical tool.

Normal mode vectors represent time-independent linear combinations of atomic displacements, with characteristic vibrational frequencies that have well-known chemical applications in infrared spectroscopy. In contrast, Lyapunov vectors represent time-dependent displacements of atomic positions and momenta with characteristic, time-dependent rates, which have applications still to be determined. They are also dynamical objects, with their own equations of motion, that represent the instantaneous directions contributing to dynamical stability and instability. Dynamical (in)stability can be measured from statistical observables associated with Lyapunov vectors, such as Lyapunov exponents.[1–4] Estimating finite-time Lyapunov exponents from numerical calculations has provided new insights into ergodicity and chaos.[5–9]

One important finding from Lyapunov exponents is that different regions of phase space may be explored on separate time scales, a phenomenon called local ergodicity. This phenomenon is reflected in multimodal finite-time Lyapunov exponent distributions collected from trajectories partitioned into shorter time segments.[10] It has only been investigated for small atomic clusters,[11] not in molecules, pointing to the potential of finite-time Lyapunov exponents and their statistics for the study of molecular reaction dynamics. This potential has not yet been fully realized.

Here we show that the rates of phase space exploration associated with minima and transition states of the potential energy surface provide a specific, quantitative, means of characterizing and identifying distinct motions. We investigate the isolated H_2O and H_3O^+ molecules and by estimating the corresponding time scales from the statistics of finite-time Lyapunov exponents, we demonstrate the utility of dynamical instability for characterizing their elementary motions. The relative degrees of chaos near saddles and minima on the potential landscape are not only an indicator of local ergodicity, but may also be useful in mapping optimal pathways for control of chemical reactions. We also anticipate that our results will have implications for more complex molecular systems.

Understanding the chaotic classical dynamics of molecules may help to understand the development of statistical behavior in molecular systems, by indicating where rapid redistribution of vibrational energy throughout a molecule occurs.[12] Similar motivation comes from the possibility of a mechanism for inducing non-statistical behavior and controlling molecular motion. The present research was further motivated by recent algorithms for the calculation of covariant, coordinate-independent Lyapunov vectors,[13] and by the fact that the associated time-dependent rates of expansion or contraction, known as finite-time Lyapunov exponents, have not been applied to molecular systems before.

The local curvature of the potential energy surface and changes in this curvature over time are key factors determining the degree of chaos, particularly over finite time

a)Electronic mail: dw34@cam.ac.uk.

spans;[14–16] this is not only true near potential energy saddles[12] but also near minima.[17] For example, the saddle region in the Lennard-Jones trimer, LJ_3, can collimate neighboring trajectories, acting as a phase space bottleneck,[18–20] thereby reducing the degree of chaos in the cluster. Our intent in the present work is to explore whether similar behavior is exhibited by one of the most important molecules, water, using a flexible empirical model; by examining neutral and protonated water in isolation, all degrees of freedom can be simulated along with the associated Lyapunov vectors.

Below, after introducing our simulation methods and the water model, we discuss our results for the chaotic dynamics of the water monomer and hydronium ion and how the potential energy curvature underlies this behavior.

II. MODEL AND METHODS

For our atomistic simulations, we adopted the reactive, interatomic potential developed by Garofalini *et al.*[21] Most classical models for the interaction between water molecules involve rigid or harmonic monomers, developed to reproduce aspects of bulk water, which prohibits studies of the dynamics and dynamical instability of certain degrees of freedom.[22] Recent all-atom, reactive, or flexible models, such as Garofalini *et al.*'s, overcome this limitation within a classical framework.

The interatomic potential is a three-center, reactive potential involving three point charges and three diffuse (Gaussian) functions centered on the nuclei. It includes two-body and three-body terms[21,22] and is entirely flexible, with full permutational symmetry. Following the recommendations in Ref. 21 for isolated molecules, we did not employ the Wolf-summation method for damping the electrostatic interactions.

Dynamics are determined by the potential energy landscape, and to complement our dynamical simulations we identified the stationary points of H_2O and H_3O^+ and the isomerization mechanisms. Configurations corresponding to potential energy minima were found by limited memory Broyden-Fletcher-Goldfarb-Shanno minimization.[23] Potential energy saddle configurations were found by a modified version of hybrid eigenvector-following[24–27] with a root-mean-square gradient termination criterion of 10^{-4} kcal mol^{-1} Å^{-1}.

We also calculated the normal modes of the minimum and saddle configurations. Analysis of normal modes (and the propagation of a tangent space basis, to be discussed shortly) required Hessian matrices, which were calculated from numerical second derivatives using central differences of the analytical gradients with a displacement of 10^{-9} Å. The six remaining eigenvalues corresponding to overall translation and rotation are zero to high precision. These degrees of freedom were not projected from the Hessian.

The stationary point normal modes served two purposes. First, normal mode vectors were used as displacements of (center-of-mass frame) global minimum equilibrium configurations to fix initial conditions for numerical trajectories. After displacement in normal mode directions, the potential energy fixed the total energy for the subsequent trajectory. Thus, the normal mode excitations were used to control the initial total energy. All the reported total energies are relative to the potential energy of the global minimum configuration. Second, the normal mode frequencies provided convenient reference points for the Lyapunov exponents.

From excited configurations, individual constant total energy trajectories were propagated forward in time through the $2s$-dimensional phase space, where s is the number of degrees of freedom. The velocity Verlet algorithm[28,29] was used to solve Hamilton's equations numerically. Trajectories were 5 ns in duration: 5×10^7 time steps with a step size of 0.1 fs. The total energy, linear momentum, and angular momentum were well conserved.

Within a linear approximation, perturbations around each phase point can be represented by vectors in tangent space, which is a copy of phase space with each phase point at the origin. Here, a basis set of orthonormal vectors, $\{\mathbf{u}_i(t_0)\}$, $i = 1, \ldots, 2s$ was defined at the initial phase point as the $2s \times 2s$ identity matrix, though any arbitrary matrix may be chosen. This tangent space basis moves in correspondence with the phase point, and when periodically orthonormalized it becomes the Gram-Schmidt vector (GSV) basis $\mathbf{G}(t) = \{\mathbf{g}_i(t)\}$ at time t. The GSVs were propagated forward in time, along with the trajectory, according to the linearized Hamilton's equations with the linearized velocity Verlet algorithm.[11,30]

The GS basis vectors $\mathbf{g}$ are $2s$-dimensional first variations of the form $(\delta\mathbf{q}, \delta\mathbf{p})^{\mathrm{T}}$. These vectors are propagated with

$$\bar{\mathbf{g}}_i(t_{j+1}) = \mathbf{M}(t_{j+1}, t_j)\,\mathbf{g}_i(t_j). \tag{1}$$

The tangent space propagator for each step $\mathbf{M}$, resulting from the linearization of the velocity Verlet algorithm,

$$\begin{pmatrix} \mathbf{I} & \mathbf{0} \\ -\frac{\tau}{2}\mathbf{H}(t_{j+1}) & \mathbf{I} \end{pmatrix} \begin{pmatrix} \mathbf{I} & \mathbf{T} \\ \mathbf{0} & \mathbf{I} \end{pmatrix} \begin{pmatrix} \mathbf{I} & \mathbf{0} \\ -\frac{\tau}{2}\mathbf{H}(t_j) & \mathbf{I} \end{pmatrix}, \tag{2}$$

is composed of $s \times s$ blocks, where $\tau = t_{j+1} - t_j$ is the time step size of 0.1 fs, $(\mathbf{T})_{kl} = \tau\,\delta_{kl}/m_k$, δ_{kl} is the Kronecker delta, $\mathbf{I}$ is the identity matrix, and $\mathbf{H}$ is the mass-weighted Hessian matrix. Because the vectors are propagated by Hessians at successive time steps, their properties are a reflection of changes in the local potential energy surface curvature.

Following each time step the GSVs are no longer orthogonal; non-orthogonal GSVs are denoted by $\bar{\mathbf{g}} = (\overline{\delta\mathbf{q}}, \overline{\delta\mathbf{p}})^{\mathrm{T}}$. Thus, at regular intervals during the trajectory, we applied the GS orthogonalization procedure to $\{\bar{\mathbf{g}}_i(t_{j+1})\}$ generating the GS vectors at the next time step $\{\mathbf{g}_i(t_{j+1})\}$. Gram-Schmidt orthogonalization is a method of implementing a QR decomposition. The QR decomposition of a general matrix $\mathbf{A}$ produces the orthogonal matrix $\mathbf{Q}$ and an upper triangular matrix $\mathbf{R}$. At each time step the $\mathbf{Q} = \mathbf{G}$ and $\mathbf{R}$ were stored and used to extract the covariant Lyapunov vectors $\{\mathbf{v}_i(t)\}$ (CLVs) with the backward propagation prescribed by the algorithm of Ginelli *et al.*[13] An alternative algorithm is that of Wolfe *et al.*[31] These vectors are coordinate-independent and covariant (i.e., at a given phase point the CLVs are mapped by the linearized dynamics into the CLVs at the next phase point of a trajectory), while the Gram-Schmidt vectors are not.[32,33]

Phase space and tangent space dynamics on any arbitrary time scale may be examined by dividing a trajectory into time segments of uniform length l. This procedure can be thought of as temporal coarse-graining. The exponents calculated in

TABLE I. Normal mode vibrational frequencies in cm^{-1} and symmetries for the Garofalini H_2O and H_3O^+ stationary points. The corresponding frequencies are in the range of 0.10 to 0.80 fs^{-1}. The H_2O linear configuration with $D_{\infty h}$ symmetry has a Hessian index of 3 and the linear configuration with $C_{\infty v}$ symmetry has an index of 2. Potential energies ΔV relative to the global minimum potential energy are shown in the last row (kcal mol^{-1}).

H_2O		
Minimum C_{2v}	Saddle $D_{\infty h}$	Saddle $C_{\infty v}$
4077.13 A_1	2665.14 Σ_g^+	4019.43 Σ^+
3986.87 B_2	−1917.66 Σ_u^+	2277.52 Σ^+
1951.57 A_1	−780.19 Π_u	−250.36 Π
$\Delta V = 0$	21.57	17.60
H_3O^+		
Minimum C_{3v}	Planar D_{3h}	
3548.86 A_1	2916.42 A_1'	
3426.26 E	2663.07 E'	
1930.44 E	1158.56 E'	
1331.43 A_1	−823.63 A_2''	
$\Delta V = 0$	5.86	

each time window are finite-time Lyapunov exponents $\lambda_i(t_l) = \lambda_i(l)$. Here, estimates of Lyapunov exponent spectra were obtained from the CLVs $\mathbf{v}_i(t)$. Each exponent was calculated from the Euclidean norm $\|\mathbf{v}_i(t)\|$, in natural logarithmic units (nats) per unit time (fs)

$$\lambda_i(t_l) \equiv \left\langle \ln \frac{\|\mathbf{v}_i(t_{j+1})\|}{\|\mathbf{v}_i(t_j)\|} \right\rangle_{t_l}, \tag{3}$$

where $\langle . \rangle_{t_l}$ is a time average over the interval $0 \le t_j \le t_l$. Finite-time properties of contiguous time segments can be averaged to examine longer time scales. In the limit of infinite time, the system is ergodic and these distributions are invariant properties of the entire phase space. Here, we show that these invariant distributions fully characterize the classical elementary motions of a water molecule.

III. RESULTS AND DISCUSSION

Water dynamics in bulk and biological environments are rich in complex, correlated motions, spanning multiple length, and time scales. In part, this behavior is determined by the elementary dynamics of individual water molecules[34–37] and clusters, prompting our examination of the chaotic dynamics of the most basic building blocks, the neutral water monomer and the hydronium ion. Furthermore, our intent is to explore the proposition that sample distributions of finite-time Lyapunov exponents, the exponential rates of expansion or contraction of the covariant Lyapunov vectors, contain subpopulations; it is these subpopulations that will characterize the elementary motions ultimately responsible for the rich behavior of bulk water.

Since the potential energy landscape determines the results from our molecular dynamics simulations, we identified stationary points, their normal mode vectors/frequencies, and the pathways connecting them (Table I).

For the Garofalini[21] water monomer there are three stationary points: the global minimum (C_{2v}) and two linear saddles. A linear, symmetric saddle (Hessian index three, $D_{\infty h}$) lies 21.57 kcal mol^{-1} higher in energy than the potential minimum and a linear, asymmetric saddle (Hessian index two, $C_{\infty v}$) lies 17.60 kcal mol^{-1} above the minimum. The energies of the global minimum, symmetric saddle, and asymmetric saddle are −215.69, −194.12, and −198.10 kcal mol^{-1}, respectively.

TABLE II. Normal mode vibrational frequencies in cm^{-1} and symmetries for the H_2O and H_3O^+ stationary points at the CCSD/6-311+G(d,p) level. Potential energies ΔV relative to the global minimum potential energy are shown in the last row (kcal mol^{-1}).

H_2O		H_3O^+	
Minimum C_{2v}	Saddle $D_{\infty h}$	Minimum C_{3v}	Planar D_{3h}
3897.08 A_1	4128.36 Σ_g^+	3654.63 A_1	3701.13 A_1'
3999.29 B_2	4515.43 Σ_u^+	3754.67 E	3847.20 E'
1655.45 A_1	−1738.83 Π_u	1701.70 E	1643.08 E'
		908.91 A_1	−692.73 A_2''
$\Delta V = 0$	32.97	$\Delta V = 0$	1.96

The saddles of the water monomer for this model are not accurate representations of the true potential energy surface, as confirmed from quantum mechanical calculations (CCSD/6-311+G(d,p) level, Table II). For bulk water simulations under normal conditions the saddles are not important, because they lie too high in energy to be accessible. For the present work we simply wish to show that Lyapunov exponent distributions characterize elementary molecular motions for the given landscape. Despite the simplicity of the Garofalini water model, the structural, dynamical, and thermodynamic data for bulk water agree well with experimental results over a temperature range of 273 to 373 K and up to a pressure of 600 MPa.[21] Furthermore, the model describes neutral, protonated, and deprotonated species and thus allows the simulation of classical proton transfer events with only a single potential function. Consequently, this model allows us to study both isolated H_2O and H_3O^+, although the stationary points of the latter system are better represented than for the neutral.

Normal mode excitations (symmetric and asymmetric stretches) of the global minima were used as initial conditions for our numerical trajectories. Sufficiently large excitations led to chaotic trajectories, mode-mode coupling, and isomerization through the linear saddles. Normal mode vibrational frequencies, calculated from the eigenvalues of the mass-weighted (Cartesian coordinate) Hessian matrix, and symmetries are reported in Table I.

Water monomer dynamics were simulated over a wide range of total energies. To probe the dynamical processes at each energy, finite-time Lyapunov exponents were collected from the time segments of these partitioned trajectories. Distributions of these exponents are shown in black in Figures 1(a)–1(c) at three total energies. These energies were fixed by the excitations of the symmetric stretch mode, though similar results were obtained for the asymmetric stretch excitations. At the arbitrarily chosen energy of 22.7 kcal mol^{-1} the water molecule is able to isomerize (the highest barrier is 21.57 kcal mol^{-1} above the minimum) and the configuration

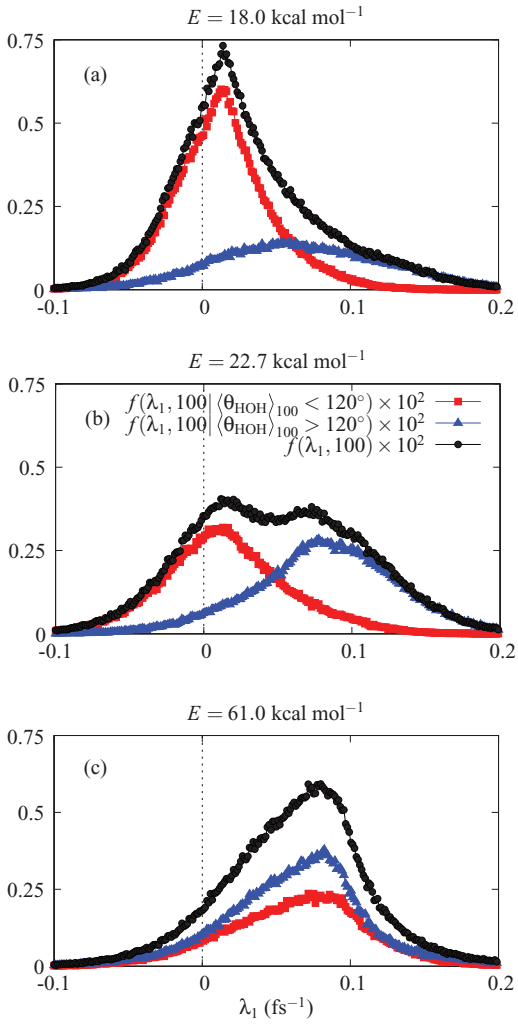

FIG. 1. Distributions $f(\lambda_1, 100)$ of three constant energy H_2O trajectories. The total energies $E =$ (a) 18.0, (b) 22.7, and (c) 61.0 kcal mol^{-1} were initially deposited in the symmetric stretch mode of the global minimum. The energy of (a) is just greater than the relative potential energy of the asymmetric saddle and that of (b) is just greater than the relative potential energy of the symmetric saddle. Trajectories were partitioned into time segments of $l = 100$ time steps or 10 fs with a 0.1 fs time step. Conditional distributions using the HOH angle, also averaged over 100 time steps, resolve the populations at lower energies where motion near the minimum and transition state is separable: (blue) $\langle \theta_{HOH} \rangle > 120^\circ$ and (red) $\langle \theta_{HOH} \rangle < 120^\circ$.

accesses the saddle region. In order to characterize the phase space flux of isomerizing trajectories, our simulations were run long enough to sample a sufficient number of isomerizations. The figure shows that even at energies just above the lowest isomerization barrier, the distribution of exponents is bimodal.

Geometries close to linear are not likely to be thermally accessible in most situations, requiring about 36 k_BT of internal energy at $T = 300$ K. Nevertheless the finite-time Lyapunov exponent sample distributions are still an interesting probe of the phase space and potential energy landscape. These distributions do have clear subpopulations, but further analysis is required to show which subpopulations are associated with which particular molecular motions. On the basis of our past work on Lennard-Jones and Morse clusters,[11,30] the peaks in exponent distributions can be associated with motion in different regions of phase space and, hence, the potential energy landscape.

To show that each peak or subpopulation reflects a different type of dynamics, the populations must be separated and identified. For this purpose we used conditional distributions of the first finite-time Lyapunov exponent. The HOH bond angle $0^\circ < \theta_{HOH} < 180^\circ$ was employed as an order parameter to identify configurations near the potential minimum and saddle. Time segments with time-averaged HOH angles greater than 120° were assigned to the transition state, while HOH angles less than 120° were assigned to the minimum. For reference, the HOH angle of the global minimum geometry in this model is 107.04°.

Conditional exponent distributions were unimodal, as shown in Figure 1 (red and blue), indicating good separation of the total distribution: at an angle less than 120° the configuration is nearer the potential minimum and at an angle greater than 120° the configuration lies closer to the linear saddle ($\theta_{HOH} = 180^\circ$). With these distributions the subpopulations can be associated with specific motions of water. In panels (a) and (b), the peak for the larger exponent is assigned to motion near the saddle, and the peak for the smaller exponent to motion around the minimum. Larger positive exponents indicate more dynamical instability and more sensitivity to initial conditions. Larger negative exponents indicate more dynamical stability and less sensitivity to initial conditions. Hence, from Figure 1, motion in the saddle region is more sensitive to the initial phase point and chaotic, while intra-well motion is more regular and ordered.

As another case study, let us now discuss the protonated water monomer (oxonium or hydronium ion), where the energy landscape exhibits a different topology. As for the ammonia molecule, there are two non-superimposable permutational isomers of the C_{3v} global minimum, connected by a planar D_{3h} transition state. The umbrella inversion involves a barrier of 5.87 kcal mol^{-1}. The initial configurations considered for the hydronium ion were also perturbations along normal modes, which led directly to umbrella inversion for sufficiently large excitations. The potential energy of the global minimum and the planar saddle (Hessian index one) are −259.03 and −253.16 kcal mol^{-1}, respectively. Vibrational frequencies and symmetries are reported in Table I.

Trajectories at total energies above the planar transition state lead to distributions of finite-time Lyapunov exponents that are again bimodal. Figure 2 shows distributions at three total energies. There are distinct peaks associated with motion in different regions of phase space. The smaller exponents correspond to motion in the potential wells of the two permutationally distinct global minima, while larger exponents correspond to motion around the transition state. Although the symmetric stretch was used to initially excite H_2O and H_3O^+, the other global minimum modes in Table I were also excited, giving similar results. Subpopulations of the finite-time Lyapunov exponent sample distributions for H_3O^+ were separable using the distance between the oxygen and the center-of-mass as an order parameter, but these results are not shown.

In general, finite-time Lyapunov exponent distributions reflect changes in the phase space. Here, the sample means and abundances of the exponent subpopulations

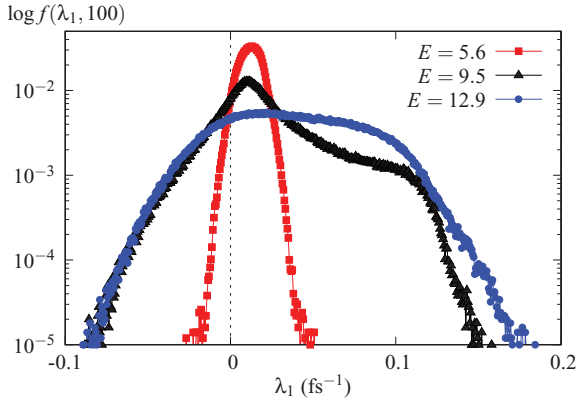

FIG. 2. Distributions of $\log f(\lambda_1, l)$ of three constant energy trajectories for H_3O^+. The total energies $E = 5.6$, 9.5, and 12.9 kcal mol^{-1} were initially deposited in the A_1 symmetry umbrella mode of the global minimum. The time segment length used to partition the trajectory was $l = 100$ time steps or 10 fs with a 0.1 fs time step.

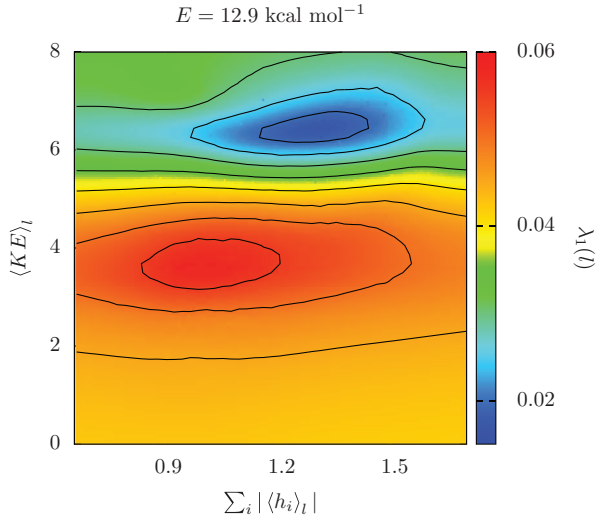

FIG. 3. Map of $\lambda_1(l = 100)$ sampled during a 5×10^7 step trajectory for H_3O^+. Exponents are plotted in terms of the time-averaged kinetic energy and sum of Hessian eigenvalue magnitudes h_i (kcal mol^{-1} Å^{-1}). All quantities are time averages over $l = 100$ time steps, 10 fs. The total energy $E = 12.9$ kcal mol^{-1} was initially deposited in the A_1 symmetry umbrella mode of the global minimum. Peaks are clearly resolved in both the kinetic energy and eigenvalue dimensions; the more chaotic peak for larger $\lambda_1(100)$ is at low kinetic energy and net potential energy curvature.

reflect changes in the local phase space regions with energy (Figure 1). With increasing total energy the mean of the total distribution shifts to larger λ. Above the potential energy of the saddle the distribution becomes bimodal and as the total energy is increased further, both means shift to larger λ. At the highest total energies accessible without inducing dissociation, the peaks merge. The traversal of the saddle at these energies is such that the time scales for exploration of the minima and saddle phase space regions are not separable, at least with the 10 fs time segment chosen to time resolve these trajectories.

Sample means of the subpopulations in the 9.5 kcal mol^{-1} distribution are approximately $\lambda_1 = 0.01$ fs^{-1} and $\lambda_1 = 0.10$ fs^{-1}. The inverse of these exponents, the finite Lyapunov times, are approximately $\lambda_1^{-1} = 100$ and 10 fs, respectively. Such time scales are related to the predictability of future motion, given uncertainty in the initial phase point; initial uncertainty in the phase point is represented here by the volume of phase space spanned by the CLVs. These Lyapunov times suggest that motion near the saddle is less predictable than motion in the potential well, an indication that trajectories passing through the transition state may "spread." This result contrasts with the "collimation" of trajectories passing over the relatively flatter saddles considered previously for small atomic clusters.[10,11,38,39]

In both H_2O and H_3O^+, peaks characterizing isomerization are associated with larger λ than those corresponding to intra-well motion. We can then conclude that as trajectories traverse these potential energy barriers, their flow is not regularized or "streamed"[11,39] but "dispersed" in the direction of the first Lyapunov vector. The finite-time Lyapunov exponents quantify the time scales for exploring different phase space regions. However, assignment of subpopulations in exponent distributions relies on the dynamics having separable time scales, being able to collect sufficient statistics, and subsequently the ability to separate subpopulations. These factors will undoubtedly complicate matters for larger systems: more time scales will lead to more overlap, long simulations are more costly, and geometric conditions will be more difficult to identify as order parameters.

However, for these small systems, abundances of each subpopulation (peak heights) quantify the amount of each motion and are reporting on the associated phase space. At every energy the height of each distribution indicates how frequently each local region of phase space was visited during the dynamical trajectory. Here, local regions of phase space are those associated with motion near the potential energy minimum and in the transition state, as determined by an order parameter (e.g., the HOH bond angle). If we assume that each phase space region is fully explored (i.e., local ergodicity[1,2]) then the peak heights also indicate the relative size of each region of phase space; furthermore, the sample means of these subpopulations are a measure of how quickly these local regions of phase space are explored.

The greater chaoticity of interwell motion (compared to motion near the saddle) deserves further discussion and analysis. Since previous results have demonstrated that traversal of flat saddles is less chaotic than intra-well motion,[10,11] we might expect that the saddles of interest here have relatively greater curvature, leading to the spreading of trajectories passing through the transition state region. However, this is not the case. Figure 3 shows a map of the first finite-time Lyapunov exponent over the trajectory as a function of both the time-averaged kinetic energy and sum of Hessian eigenvalues h_i over the same time span. In this map larger exponents are associated with time intervals in which the kinetic energy and net potential energy curvature, as indicated by the Hessian eigenvalues, are low.

Collimation of neighboring trajectories in saddle regions leads to smaller exponents, but it requires decoupling of the reaction coordinate from the remaining degrees of freedom.

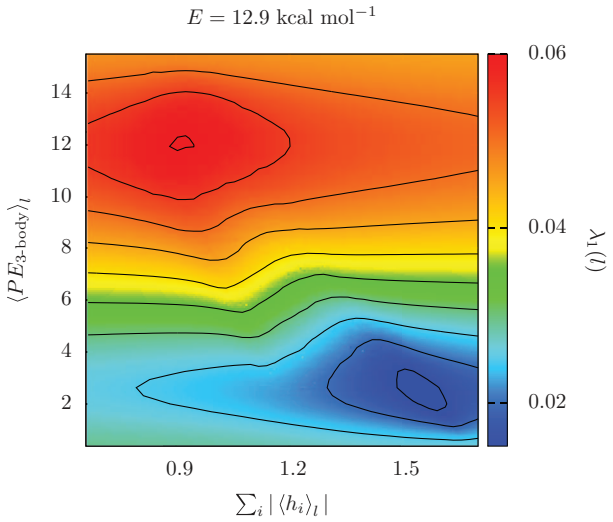

FIG. 4. Map of $\lambda_1(l = 100)$ sampled during a 5×10^7 step trajectory for H_3O^+. Exponents are plotted in terms of the time-averaged three-body potential energy and sum of Hessian eigenvalue magnitudes h_i (kcal mol^{-1} Å^{-1}). All quantities are time averages over $l = 100$ time steps, 10 fs. The total energy $E = 12.9$ kcal mol^{-1} was initially deposited in the A_1 symmetry umbrella mode of the global minimum. The more chaotic peak, corresponding to larger $\lambda_1(100)$, is at large values of the three-body potential energy and low net potential energy curvature.

Our results demonstrating the spreading of neighboring trajectories near saddles suggest that the reaction coordinate is not separable in this model. Theoretical support for our numerical simulations and the above inference has recently come from Lorquet,[40] who specified three necessary conditions for decoupling of a reaction coordinate from the remaining "bath" modes: nonresonance between the bath mode frequencies, smooth anharmonic perturbations, and perturbations that are not too strong.

The last condition is not satisfied for H_2O and H_3O^+ for the Garofalini potential. In the model there is strong anharmonic coupling between the degrees of freedom resulting from a three-body potential term. So, while saddles of these molecules are relatively flat (i.e., the saddles have less net curvature relative to their respective minima; see Figure 4), the reaction coordinate does not decouple from the other degrees of freedom. In agreement with Lorquet's theoretical analysis, Figure 4 shows that the highest three-body potential energy term is associated with the largest positive λ_1 and the lowest net curvature. We note that the Lennard-Jones model has no three-body interactions capable of affecting chaotic behavior. Although finite-time Lyapunov exponents are used as the only criteria for chaotic behavior near the saddles, the action in the reaction coordinate is expected to be a comparable measure;[11,38,39] however, a proper comparison of these two criteria will require further investigation.

Another interesting aspect of our findings comes from an examination of the first CLV in the time segments that gave exponents corresponding to the peak maxima in Figures 1 and 2. Representative atomic position vectors (projected from the first CLV in this time segment) and the configurations to which they correspond are shown in Figure 5. Configurations associated mostly with the saddle region give the

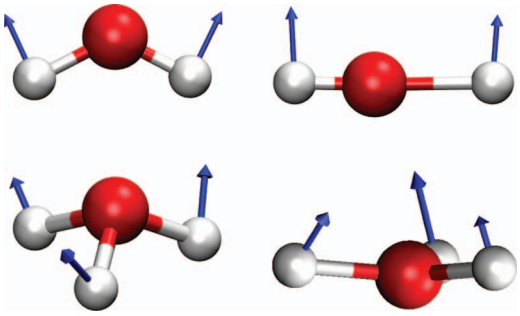

FIG. 5. Representative instantaneous atomic configurations of H_2O (top) and H_3O^+ (bottom). Also shown are the three-component displacement vectors of the first CLV. Snapshots correspond to time segments where finite-time Lyapunov exponents were near maxima in the bimodal distributions. Note that the vectors associated with hydrogens are much larger in magnitude than those associated with oxygen.

larger-exponent peaks. Those corresponding to minima give the smaller-exponent peak. We also note that for many time segments, the hydrogen atomic coordinate vectors were found to be longer and are likely the largest contributors to the dynamical instability, as expected from the isomerization mechanisms.

Our simulations for two small molecules have only illustrated some of the power in the method. First, simulated trajectories are long enough to fill the energetically accessible phase space and provide sufficient samples for finite-time exponent distributions, each exponent being calculated over a segment of a uniformly partitioned trajectory. The exponent distributions are then a property not only of the dynamics (i.e., motion around the potential energy minimum or the isomerization saddle) but also the different regions of phase space. Second, Lyapunov exponents are a useful diagnostic for identifying the invariants of a molecular dynamical trajectory, assessing the stability of simulated trajectories, and potentially gauging the quality of classical molecular models.

Distinct peaks in finite-time exponent distributions are specific to elementary molecular motions, where the water monomer approaches linearity and the hydronium ion undergoes Walden inversion. These peaks may be used to complement ultrafast infrared spectroscopy, indicating which regions of phase or configuration space are most (least) chaotic and least (most) controllable. In more complex systems, capable of motion through multiple min-ts-min sequences, the peak intensities may give the probability for a particular dynamical process (e.g., isomerization), allowing the determination of the dynamically relevant transition states or reaction pathways.

IV. CONCLUSIONS

This analysis of the finite-time exponents (from covariant Lyapunov vectors) for three- and four-atom molecules with single- and double-well potential energy landscapes demonstrates the emergence of local ergodicity for a flexible molecular model. As for Lennard-Jones clusters,[11,39] separate time scales for phase space exploration in H_2O and H_3O^+ are apparent from the appearance of subpopulations in finite-time Lyapunov exponent distributions. These subpopulations are

useful dynamical spectral identifiers for specific motions of isolated molecular species. Unlike Lennard-Jones clusters, the motion involved in transition states is more chaotic and less predictable than motion near potential minima.

The present results for two molecules, with a particular model potential, show that Lyapunov vectors and their exponents are a response to changes in curvature of the potential energy landscape, though the connection is subtle. We believe that exponent distributions are useful as a predictive, quantitative tool for interpreting chaotic molecular dynamics. The full generality and power of this method has yet to be fully established. One obstacle to future development is that the peaks in these distributions would overlap and need to be resolved in more complex systems. However, the possibility to inform control and predictability of molecular motion with ultrafast spectroscopy seems very promising.

ACKNOWLEDGMENTS

J.R.G. acknowledges support from the National Science Foundation (NSF) (Grant No. OISE-0700911), the computational resources of CamGrid, and technical assistance from Dr. Mark Calleja. R.S.B. acknowledges the hospitality of the Aspen Center for Physics, where much of his contribution was made.

[1]C. Amitrano and R. S. Berry, Phys. Rev. Lett. **68**, 729 (1992).
[2]C. Amitrano and R. S. Berry, Phys. Rev. E **47**, 3158 (1993).
[3]H. Fujisaka, Prog. Theor. Phys. **70**, 1264 (1983).
[4]J.-P. Eckmann and D. Ruelle, Rev. Mod. Phys. **58**, 617 (1985).
[5]H. Posch and W. Hoover, J. Phys.: Conf. Ser. **31**, 9 (2006).
[6]R. S. Berry, Adv. Chem. Phys. **130**, 3 (2005).
[7]M. A. Sepúlveda, R. Badii, and E. Pollak, Phys. Rev. Lett. **63**, 1226 (1989).
[8]A. Prasad and R. Ramaswamy, Phys. Rev. E **60**, 2761 (1999).
[9]B. Eckhardt and D. Yao, Physica D **65**, 100 (1993).
[10]D. J. Wales and R. S. Berry, J. Phys. B **24**, L351 (1991).
[11]R. J. Hinde, D. J. Wales, and R. S. Berry, J. Chem. Phys. **96**, 1376 (1992).
[12]R. J. Hinde and R. S. Berry, J. Chem. Phys. **99**, 2942 (1993).
[13]F. Ginelli, P. Poggi, A. Turchi, H. Chaté, R. Livi, and A. Politi, Phys. Rev. Lett. **99**, 130601 (2007).
[14]P. Brumer and J. W. Duff, J. Chem. Phys. **65**, 3566 (1976).
[15]M. Toda, Phys. Lett. A **48**, 335 (1974).
[16]R. Kosloff and S. A. Rice, J. Chem. Phys. **74**, 1947 (1981).
[17]L. Casetti, M. Pettini, and E. G. D. Cohen, Phys. Rep. **337**, 237 (2000).
[18]S. K. Gray, S. A. Rice, and M. J. Davis, J. Phys. Chem. **90**, 3470 (1986).
[19]M. J. Davis and S. K. Gray, J. Chem. Phys. **84**, 5389 (1986).
[20]C. C. Martens, M. J. Davis, and G. S. Ezra, Chem. Phys. Lett. **142**, 519 (1987).
[21]T. S. Mahadevan and S. H. Garofalini, J. Phys. Chem. B **111**, 8919 (2007).
[22]B. Guillot, J. Mol. Liq. **101**, 219 (2001).
[23]J. Nocedal, Math. Comput. **35**, 773 (1980).
[24]L. J. Munro and D. J. Wales, Phys. Rev. B **59**, 3969 (1999).
[25]G. Henkelman and H. Jónsson, J. Chem. Phys. **111**, 7010 (1999).
[26]Y. Kumeda, L. J. Munro, and D. J. Wales, Chem. Phys. Lett. **341**, 185 (2001).
[27]A. Heyden, A. T. Bell, and F. J. Keil, J. Chem. Phys. **123**, 224101 (2005).
[28]W. C. Swope, H. C. Andersen, P. H. Berens, and K. R. Wilson, J. Chem. Phys. **76**, 637 (1982).
[29]L. Verlet, Phys. Rev. **159**, 98 (1967).
[30]J. R. Green, J. Jellinek, and R. S. Berry, Phys. Rev. E **80**, 066205 (2009).
[31]C. L. Wolfe and R. M. Samelson, Tellus **59A**, 355 (2007).
[32]H. Bosetti, H. A. Posch, C. Dellago, and W. G. Hoover, Phys. Rev. E **82**, 046218 (2010).
[33]H. liu Yang and G. Radons, Phys. Rev. E **82**, 046204 (2010).
[34]G. S. Ezra, "Dynamics of small solar system bodies and exoplanets," in *Intramolecular Dynamics and Nonlinear Dynamics*, edited by W. L. Hase (JAI, Greenwich, CT, 1992), pp. 1–40.
[35]B. G. Sumpter and G. S. Ezra, Chem. Phys. Lett. **142**, 142 (1987).
[36]R. T. Lawton and M. S. Child, Mol. Phys. **37**, 1799 (1979).
[37]R. C. Mayrhofer and E. L. Sibert, Theor. Chim. Acta **92**, 107 (1995).
[38]T. Komatsuzaki and R. S. Berry, Proc. Natl. Acad. Sci. U.S.A. **98**, 7666 (2001).
[39]T. Komatsuzaki and R. S. Berry, J. Chem. Phys. **110**, 9160 (1999).
[40]J. C. Lorquet, J. Phys. Chem. A **115**, 4610 (2011).